Ethanol dehydrogenation to acetaldehyde with mesoporous Cu-SiO_2 catalysts prepared by aerosol-assisted sol-gel

Giovanni Pampararo[1,2], *Gabriella Garbarino*[3,4*], *Paola Riani*[1,4], *Vit Vykoukal*[5], *Guido Busca*[3,4], *Damien P. Debecker*[2,*]

Corresponding authors: Damien.Debecker@uclouvain.be, gabriella.garbarino@unige.it

1. University of Genova, DCCI Department of Chemistry and Industrial Chemistry, Via Dodecaneso 31, 16146, Genova, Italy
2. Université catholique de Louvain (UCLouvain), Institute of Condensed Matter and Nanosciences (IMCN), Place Louis Pasteur, 1, 1348 Louvain-la-Neuve, Belgium
3. University of Genova, DICCA, Department of Civil Chemical and Environmental Engineering, Via all'Opera Pia 15, 16145, Genova, Italy
4. INSTM, UdR di Genova, via Dodecaneso 31, 16146, Genova, Italy
5. Department of Chemistry, Faculty of Science, Masaryk University, Kotlarska 2, CZ-61137 Brno, Czech Republic

Keywords: Ethanol dehydrogenation, Copper based catalysts, aerosol-assisted sol-gel process, mesoporous materials

Abstract:

Copper based catalysts are central for carrying dehydrogenation reactions. However, these materials are prone to deactivation by sintering and coke deposition. Irreversible sintering occurring during reaction (under the effect of temperature) is known to decrease both activity and selectivity, where the unwanted dehydration activity of the support might also play an important role. From this perspective, the quite unreactive silica supports may be attractive. However, using classical catalyst preparation methods (e.g. impregnation), it is a challenge to obtain a stable and homogeneous dispersion of Cu over SiO_2 owing to the weak support-active phase interactions. Taking a sidestep, aerosol-assisted sol-gel is a promising alternative for the facile preparation of mesostructured metallosilicates with high metal dispersion. Here we report, for the first time, Cu-SiO_2 made by the aerosol-assisted sol-gel method and exploited in the ethanol non-oxidative dehydrogenation to acetaldehyde. These catalysts are compared with a series of catalysts made by impregnation to investigate, through a thorough characterization survey, the effect of the synthesis procedure as well as the effect of Cu loading. We show that aerosol-made catalysts do not suffer heavy sintering, reach high ethanol conversions with acetaldehyde selectivity above 75%, and only slowly deactivate upon time due to a (reversible) coking phenomenon.

1. Introduction

Nowadays, many efforts are being pursued to reduce our dependence on fossil ressources consumption and to obtain chemicals and fuels from renewable resources. In this field, bioethanol is a prominent platform chemical that can be produced from non-edible biomass feedstocks through fermentation [1]. Further upgrading of bioethanol gives access to several important chemical intermediates [2,3] such as ethylene, acetaldehyde, acetone and hydrogen. Certainly, acetaldehyde is an important target that can then be further transformed to produce valuable fine and bulk chemicals such as carboxylic acids, ketones, and esters [4]. Industrially, it is produced via the well-established Wacker-Hoechst process (oxidizing ethylene to acetaldehyde in the presence of an aqueous solution of palladium chloride and copper chloride). Suitable alternatives – starting from bioethanol – are desirable but stable and robust catalysts for this application are still lacking [5].

Noble and non-noble metal based catalytic systems have been widely studied for this reaction, and copper appears as the most suitable compromise when considering performances on the first hand and metals availability and price on the second hand [6]. Bueno et al. [7–9] reported that the catalytic activity of Cu-ZrO_2 materials depends strongly on Cu nanoparticles size and on their interaction with the support. Hanukovich et al. [10] observe that Cu surface over ZrO_2, TiO_2, $AlZrO_2$ supports becomes poisoned with reactive intermediates, pointing out the need to choose support with moderate Lewis acidity, to avoid the formation of side products that trigger fouling. Copper-based catalysts supported on Al_2O_3, $ZnAl_2O_4$, $MgAl_2O_4$, $Zn_xMg_yAl_2O_z$ have also been investigated [11–16]. These catalysts are active and selective to acetaldehyde (>90%) also at high conversion, but a progressive deactivation appears inevitable, owing to an interplay between Cu sintering and carbon deposition [17]. While sintering is an irreversible effect, mild oxidative treatments could efficiently rejuvenate the catalysts by burning carbonaceous residues. Carbon supported Cu- catalysts [18–20] showed good activity levels at 623 K, but dehydration reactions - mainly associated with the presence of oxygen-containing acidic groups on the carbon surface – limit the selectivity of the reaction.

Silica-supported Cu-based catalysts are reported as highly selective to acetaldehyde because of the relative inertness of silica towards side reactions such as dehydration [21]. Thus, Cu/SiO_2 catalysts are also suitable model materials to study the behaviour of Cu nanoparticles [9,22–24]. Using such approach, a marked structure-relationship was demonstrated [25]. Cu particle size strongly influence selectivity because it dictates the density of (catalytically active) coordinatively unsaturated sites, such as corners and kinks. Nanoparticles around 10 nm have been found to be an optimum for acetaldehyde production while larger particles seem to favour side products such as ethyl acetate [26]. Unfortunately, achieving high active phase (Cu) dispersion on silica is complicated with classical synthesis methods and intricate grafting or colloidal catalyst synthesis procedures have to be implemented [27–29]. Moreover, these catalysts remain subject to deactivation by coking and are very prone to deactivation by Cu sintering [30]. Silica, indeed, as a non-reducible oxide-support, is known to establish only weak interactions with supported metal nanoparticles, and the latter are therefore particularly prone to sintering [31]. Thus, controlling active phase dispersion and strengthening the interaction with the support is difficult, in particular when applying conventional impregnation methods on pre-formed silica supports. Therefore, the development of new synthetic procedures allowing to (i) control active site speciation and dispersion and (ii) achieve suitable morphological and textural properties [32] is needed.

Along this line, the aerosol-assisted sol-gel process (AASG) – which is emerging as a powerful route to produce various nanomaterials and in particular tailored heterogeneous catalysts [33,34] – is primed to solve the above-mentioned challenges. The method is based on the atomization and fast reactive drying of a precursor's solution. During processing, inorganic polycondensation reactions take place very rapidly, possibly coupled with the templating action of a sacrificial pore-generating agent. This allows the one-step and continuous production of nanomaterials with desired properties. Aerosol processes have been used to develop catalysts for a wide range of reactions, such as Mo-based catalysts for olefin metathesis [35], TiO_2 catalyst supports for CO_2 methanation [36], Cu-based materials

for CO_2 hydrogenation to methanol [37], Au based catalysts for CO oxidation [38] or RuO_2 based catalysts for electrocatalysis [39]. While this technique has never been used to synthesize Cu-based catalysts for ethanol non-oxidative dehydrogenation, we surmised that the control offered in terms of Cu dispersion and texture could offer decisive advantages regarding intrinsic activity and stability. Moreover, it must be recalled that aerosol processes are continuous, low-waste, and easily scalable[33].

The present work aims at exploiting Aerosol Assisted Sol Gel process (AASG) to prepare low loading Cu-based catalysts for (bio)ethanol dehydrogenation. These new catalysts are compared with conventional impregnated catalysts. With the teachings gained from the deep characterisation of fresh and used catalysts we identify the key parameters that govern the high activity of the AASG-made catalysts, and we identify the causes of deactivation and suitable rejuvenation procedures.

2. Experimental section

2.1 Catalysts preparation

Copper-based catalysts have been synthesized following two different procedures: one-step aerosol-assisted sol-gel (AASG) and incipient wetness impregnation (IWI) of pre-synthesized silica support.

2.1.1 One-pot preparation of Cu-SiO_2 by AASG technique

Solution A is prepared by mixing 0.977 mol of ethanol (VWR, >99.8 v/v%), 0.444 mol of distilled water and 0.0003 mol of Pluronic® F127 (Sigma Aldrich, ≃ 12600 g/mol)]. A second solution (B) is prepared by mixing 0.057 mol of TEOS (TCI Chemicals, >97.0%), 0.548 mol of an aqueous HCl solution with a pH=2 obtained by dilution of fuming HCl (Roth, 37 wt.%). After preparation, solution A and B were stirred overnight and then mixed together. $Cu(NO_3)_2{*}2.5\ H_2O$ was added in the desired amount to obtain the targeted Cu loading. The obtained solution was then sprayed with an atomizer, supplied by "TSI incorporated®", by applying an air pressure of 207 kPa. The aerosol droplets were dried by passing through a quartz tube heated by a tubular furnace set at 723 K. Then, the dried

material was collected on a nitrocellulose filter (Sartorius Stedim, 0.45 μm). Powders were calcined in a muffle furnace under static air, first at 623 K (1 K min^{-1}) for 3 h, and then at 823 K (1 K min^{-1}) for an additional 3 h. These catalysts were denoted as A-CuXSi, where X corresponds to the nominal Cu loading on support basis and X = 2, 5, 7.4 and 9.1 wt.%.

2.1.2 Cu/SiO_2 catalysts prepared by impregnation

Reference catalysts were prepared by incipient impregnation, using a silica support obtained by AASG. The latter was prepared by the same protocol as the CuXSi catalysts but omitting the addition of Cu nitrate. Here, copper is introduced onto the preformed silica support by wetting the latter with an aqueous solution of $Cu(NO_3)_2$*2.5 H_2O (Alfa Aesar, 98 wt.%). The amount of employed water corresponded to the volume of the support pores, evaluated by N_2 physisorption, incremented by a 20% v/v. Powders have been dried and calcined with the same protocol described above. These catalysts were denoted as I-CuXSi, where X corresponds to the nominal Cu loading on support basis and where I stands for "impregnation".

2.2 Materials Characterization

Textural properties were measured by N_2 -physisorption at 77 K using a Micrometrics Tristar 3000 instrument. Prior to analysis, calcined samples were degassed overnight under vacuum at 443 K. The Brunauer-Emmett-Teller (BET) model was used to determine the Specific Surface Area (SSA, m^2/g) in the relative pressure range of 0.05–0.30. Total pore volume (V_p) was estimated from the adsorption branch of the isotherm at p/p_0=0.98 and the average pore diameter (D_p) was estimated from the BJH model applied on the adsorption isotherms.

XRD analysis was carried out by means of a Bruker D8 Advance diffractometer (Bragg–Brentano geometry) on both fresh and spent catalysts. The diffractometer works with a Cu Kα source (λ=0.15418 nm) at 1200 W (30 mA, 40 kV). Diffraction patterns have been acquired by setting the following parameters: 2θ range 5°-100°, step size 0.05° (2θ) and 1.5 s each step. The detector was a

137 Bruker Lynxeye XE-T. Identification of the phases was carried out using Pearson's Crystal Database
138 [40]. Crystallites sizes of CuO and of Cu have been evaluated on the most intense peak by Scherrer
139 formula, via DIFFRAC.EVA V4.2.1 software. For CuO, peak at 2θ = 35.66 has been considered, for
140 Cu, peak at 2θ = 43.40 has been considered.

141 ICP-AES analyses were performed on an ICP Thermo Scientific 6500 instrument after dissolution of
142 samples (≃100 mg) by metaborate Li - tetraborate Li fusion.

143 Scanning Electron Microscope Zeiss SUPRA 40 VP, equipped with a field emission gun (FE-SEM)
144 was used to investigate sample morphology and composition for both fresh and spent catalysts. This
145 microscope is equipped with a high sensitivity "InLens" secondary electron detector and with a EDX
146 (Energy Dispersive X-Ray) Spectrometer OXFORD "INCA Energie 450 × 3". Samples were
147 suspended in ethanol. A drop of the resultant mixture was deposited on a Lacey Carbon copper grid
148 and the dried sample was then imaged.

149 Samples composition was investigated by using a scanning electron microscope (SEM) Zeiss Evo 40
150 equipped with a Pentafet Link Energy Dispersive X-ray Spectroscopy (EDXS) system managed by
151 the INCA Energy software (Oxford Instruments, Analytical Ltd., Bucks, U.K.). Samples powders
152 were directly mounted on a high purity conductive double sided adhesive carbon tab.

153 TEM and STEM-EDS measurements were carried out on a FEI Titan Themis instrument with a
154 combination of a spherical aberration image (Cs) corrector, a monochromator system, sensitive
155 ChemiSTEM technology, and a high-end GATAN GIF Quantum Energy Filter for EELS and EFTEM
156 with a new enhanced piezo stage, FEI and GATAN software, and a FEI Ceta 16-megapixel CMOS
157 camera. Powders have been dispersed in cyclohexane and 4 μL deposed on a gold grid covered by
158 QuantiFoil® holey carbon and then dried in air.

159 X-ray photoelectron spectroscopy (XPS) analyses were carried out at room temperature with an SSI-
160 X-probe (SSX 100/206) photoelectron spectrometer from Surface Science Instruments (USA),

equipped with a monochromatic Al K X-ray microfocused source (1486.6 eV). Samples were deposed onto small sample holders with adhesive tape and then placed on an insulating ceramic carousel (Macor®, Switzerland). Charge effects were avoided by placing a nickel grid above the samples and using a flood gun set at 8 eV. The binding energy scale was calibrated by fixing the Si 2p peak at 103.5 eV [41]. Data treatment was performed using the CasaXPS program (Casa Software Ltd., UK). The peaks were decomposed into a sum of Gaussian/Lorentzian (85/15) after subtraction of a Shirley-type baseline.

Infrared (IR) spectra have been obtained with a Nicolet 380 Fourier Transform IR spectrometer. Sample powders were pressed into thin wafers with KBr and spectra were recorded in air (0.5 wt% sample in KBr). Spectra have been collected with 100 scans with a resolution of 2 cm^{-1}.

DR-UV–vis-NIR spectra were collected with a JASCO V570 instrument equipped with an integrating sphere. The powders were gently pressed in the sample holder.

H_2 Temperature Programmed Reduction (TPR) measures were conducted using a CATLAB instrument, from Hiden equipped with QGA mass spectrometer for gas analysis. 55 mg of sample were loaded in a quartz reactor. First the sample was maintained at 373 K for 1 hour under flowing argon (40 mL/min). Next, the samples were exposed to a 1% H_2 flow in argon (40 mL/min) and then heated up to 873 K using a heating rate of 5 K/min. The H_2 uptake is calculated by integration of the H_2 consumption profiles. Signal intensities were referenced to the calibrated signals for known volumes of analyzed gases.

NH_3 Temperature programmed Desorption (TPD) measurements were conducted in the same CATLAB instrument. 40 mg of powders were loaded in a quartz reactor. A reductive pretreatment was carried out for 30 min at 573 K, under a 30 mL/min 5 vol. % H_2 in argon. For silica and the zeolite catalyst employed as acid benchmark, the hydrogen pretreatment was not applied. Next, the samples were cooled to 333 K under inert atmosphere. Then they are exposed to a 2 vol. % NH_3 in argon (30 mL/min) flow for 1 hour, and then flushed under argon (30 mL/min) at 333 K for 60 min.

186 The temperature-programmed desorption was carried out up to 1023 K with a ramping rate of 10 K
187 /min in a 30 mL/min flow of Ar. The NH_3 quantification was made by integration of the desorption
188 profile. Signal intensities were referenced to the calibrated signals for known volumes of analyzed
189 gases.

190 Spent catalysts were studied by thermo-gravimetry, using a TGA/DSC 3+ apparatus from Mettler-
191 Toledo, coupled with a Pfeiffer Vacuum ThermoStar^{TM} mass spectrometer. Samples (≃ 20 mg) were
192 placed in alumina crucibles (70 µL) and heated at 10 K min^{-1} from room temperature to 1173 K under
193 a dry air flow (100 mL/min). The following m/z have been recorded over the whole experiment: 28
194 (N_2), 18 (H_2O), 32 (O_2) and 44 (CO_2).

195 *2.3 Ethanol dehydrogenation to acetaldehyde*

196 Catalytic tests were carried out in a fixed bed reactor (stainless steel, 0.6 cm internal diameter). 50
197 mg of calcined catalysts (pressed, crushed and sieved in the 0.20–0.40 mm range) were diluted with
198 glass beads (0.5–1.0 mm), by keeping a constant catalytic bed volume. Before reaction, catalysts were
199 pre-reduced in situ by feeding hydrogen (20 vol.% H_2 in N_2, total flow rate of 175 mL/min) for 30
200 min at 573 K with a ramping rate of 5 K min^{-1}. Then, the reactor was set at the desired reaction
201 temperature (473 K) and the reaction feed was introduced: absolute ethanol was fed through a syringe
202 pump (NE-300) in a stream on N_2, achieving the desired molar fraction in the gas phase (2.5% mol,
203 total flow rate of 120 mL/min). All measures were carried out at atmospheric pressure while
204 temperatures were increased in a stepwise manner, from 473 K to 673 K. Every temperature step was
205 kept for 1 hour, ensuring steady state conditions. Effluent gas was analysed online with a VARIAN
206 3800 Gas Chromatograph (Varian Medical Systems, Machelen, Belgium). Four injections were made
207 at each temperature. The injector was set at 423 K and the GC was equipped with a flame ionization
208 detector (FID) kept at 463 K, a Restek Rt-U-BOND column (30 m long, internal diameter of 0.32
209 mm, film thickness of 10 µm) and a programmable oven (setup: 383 K for 5 minutes, then to 423 K
210 with a ramping rate of 5 K/min, dwelled for 5 minutes).

211 Stability tests on A-Cu7.4Si and I-Cu7.4Si have been carried out at 573 K for 8 hours in the same
212 conditions. In the case of A-Cu7.4Si catalysts, only 40 mg of catalyst was introduced in order to have
213 iso-conversion comparison with the impregnated catalyst (I-Cu7.4Si)

214 Ethanol conversion (X_{EtOH}) is defined as:

215 $$X_{EtOH} = (n_{EtOH(in)} - n_{EtOH(out)})/n_{EtOH(in)} \quad (1)$$

216 selectivity to product i is defined as:

217 $$S_i = n_i/(\nu_i(n_{EtOH(in)} - n_{EtOH(out))}) \quad (2)$$

218 And yields are defined as:

219 $$Y_i = n_i / \nu_i \, n_{EtOH(in)} \quad (3)$$

220 where n_i is the molar flow of compound i, and ν_i is the ratio of stoichiometric reaction coefficients.
221 The error in the steady state carbon balance is ± 5%.

222 *2.4 Regeneration test*

223 After the stability test (8 h at 573 K) an oxidation step was carried out by flowing a gaseous stream
224 (50 mL/min) of 20 vol % O_2 in N_2. Temperature was raised with a ramping rate of 5 K min^{-1} up to
225 788 K, and then dwelled for 15 minutes. After cooling down up to room temperature, the catalyst has
226 been tested again in the same experimental conditions.

227

228 **3. Results and discussion**

229 *3.1 Catalysts characterisation*

230 The copper content has been experimentally verified by ICP-AES (Table 1). Experimental data are
231 in good agreement, even if the observed loading is slightly lower than the nominal one (for both

aerosol-made catalysts and impregnated catalysts), suggesting a contribution of the hygroscopic properties of the metal precursor used in the preparation.

Nitrogen physisorption curves (Figure 1A, C) revealed that all the calcined catalysts showed Type IV isotherms indicating the presence of open mesopores. The shape of the hysteresis loop corresponds to the H2-type (asymmetrical with a steeper desorption branch than the adsorption one) characteristic of restrictions within the porous network. The forced closure of the hysteresis loop at p/p_0 values of 0.4–0.5 indicated the presence of mesopores smaller than ~ 4 nm [42]. The Barrett-Joyner-Halenda (BJH) model applied on the adsorption branch (Fig. 1B, D) of the isotherm revealed the presence of mesopores in the 6-12 range (centred at about 8 nm) for all catalysts. The nitrogen uptake at low relative pressure also indicates the presence of micropores whose contribution remains relatively small, as underlined by textural values summarised in Table 1.

Table 1: Composition and textural properties of catalysts prepared via IWI (I) and in one step via the AASG process (A).

Sample	Cu wt.% - ICP-AES	Surf. area [$m^2 \cdot g^{-1}$]	V_p [a] [$cm^3 \cdot g^{-1}$]	V_{micro} [b] [$cm^3 g^{-1}$]	D_p [c] [nm]
A-SiO_2	/	380	0.45	0.06	7
I-Cu2Si	1.3	329	0.44	0.05	7
I-Cu5Si	3.9	300	0.37	0.03	7
I-Cu7.4Si	6.4	290	0.54	0.03	11
I-Cu9.1Si	8.0	297	0.40	0.03	7
A-Cu2Si	1.6	505	0.70	0.09	9
A-Cu5Si	3.6	458	0.42	0.11	6
A-Cu7.4Si	6.7	458	0.62	0.10	8
A-Cu9.1Si	8.2	418	0.66	0.09	9

[a] Total pore volume, estimated from the adsorption branch of the isotherm at p/p0=0.98. [b] Microporous volume, estimated from the t-plot. [c] Average pore diameter, estimated from the BJH model applied on the adsorption isotherms.

The specific surface area (SSA) and pore volume were generally higher for A-catalysts (prepared via the one-pot AASG process), reaching as high as 505 m^2/g for A-Cu2Si. Interestingly, the micropore volume appears to be more important for one pot catalysts than for bare silica or impregnated materials. A possible explanation is related to the direct introduction of copper nitrate in the formation of A-CuX catalysts, trapped in the porous structure during the rapid droplet's condensation and drying step. Since Cu^{2+} ionic radius is -larger than that of Si^{4+}, it is possible that the silica network rearranges to host copper species, creating roughness at the surface. Alternatively, nitrates may behave as a "foaming agent" during calcination creating a family of smaller pores upon the departure of NO_x species. Upon increase in copper loading, specific surface area and pore volume tend to decrease, which is logical, considering the fact that the fraction of low-SSA Cu NP increases at the expense of the fraction of high-SSA silica.

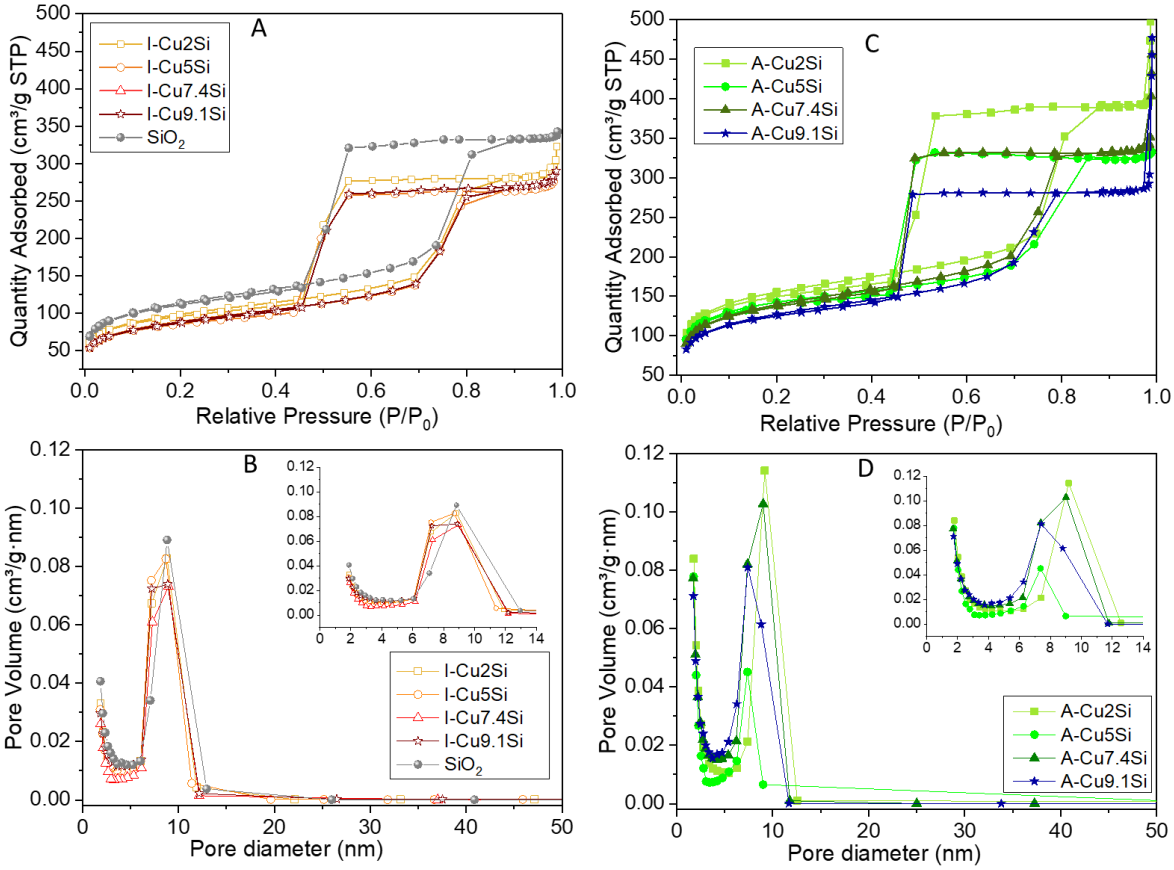

Figure 1: N_2 adsorption/desorption isotherms (insets A and C) and pore size distributions (B and D) of investigated catalysts.

The diffraction patterns were recorded for all fresh catalysts (Figure 2A and 2B). For both I-CuXSi and A-CuXSi series of catalysts, a broad diffraction peak at about 2Θ = 22° is attributed to the amorphous silica support [43]. In all catalysts having a Cu content equal or higher than 5 wt.%, the CuO phase (tenorite, mS8; PCD ref. 1243879)[40], is observed. Expectedly, the CuO diffraction peaks intensity increases with the increasing copper content in the catalyst. The Scherrer equation, applied on the most intense CuO peak at 2Θ = 35.6°, indicates an average crystallite size of 32-33 nm for both I-Cu7.4Si and I-Cu9.1Si samples. In the XRD patterns of samples obtained by AASG synthetic procedure (Fig. 2 B), the peaks intensity of CuO phase is lower; in fact, only the two main peaks, at 2Θ=35.8° and 38.8°, are visible and broader than those observed for I-CuXSi series. For A-Cu7.4Si

and A-Cu9.1Si, the crystal size evaluation with Scherrer equation leads to an average size of about 10 nm. For low loading catalysts, it is only possible to hypothesize the presence of nanoparticles with an average size equal or lower than 10 nm, hypothesis that is consistent with TEM images (see below and ESI).

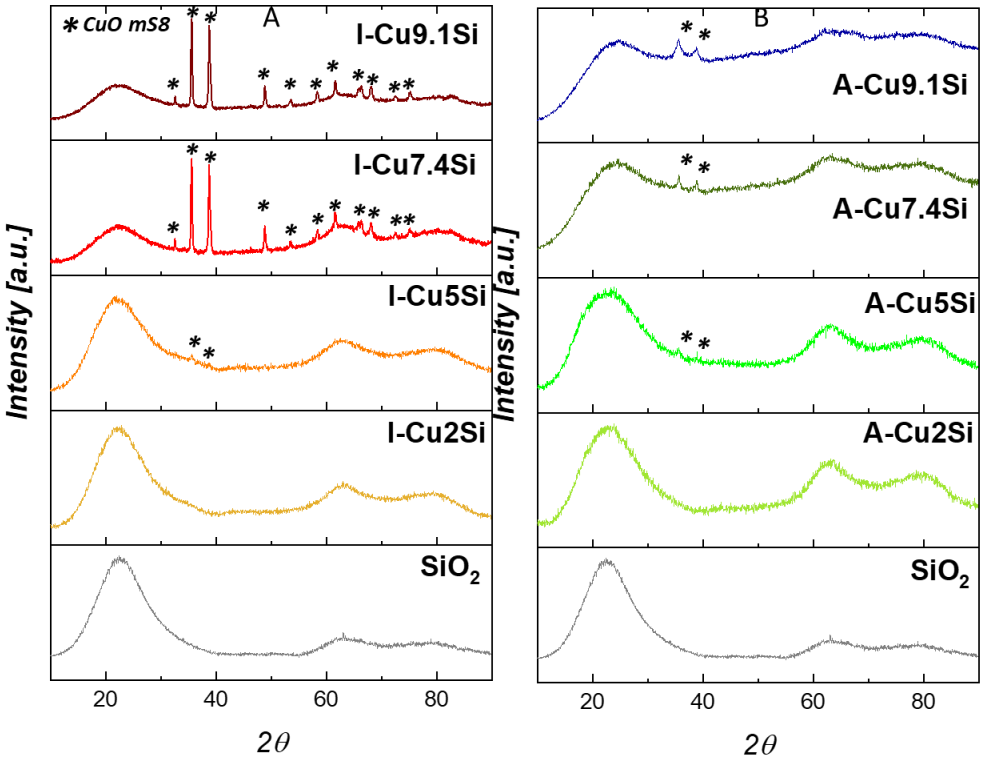

Figure 2: XRD patterns of the fresh I-samples (inset A), and A-samples (inset B). Please note that broad and weak peaks around 2Θ = 63° and 79° are attributable to the fixing agent used in the sample preparation for the analysis.

FE-SEM images of bare silica support shows spherical silica particles, with diameters between 0.1 – 5 μm (Figure 1S(A)). The obtained spherical shape is a reminiscence of the synthetic procedure that relies on a drying step of spherical aerosol droplets. In low loading impregnated catalysts i.e., I-Cu2Si and I-Cu5Si, no bright crystalline aggregates have been detected (Figure 1S(B) and (C)). At higher loading i.e., I-Cu7.4Si and I-Cu9.1Si, bright crystals are clearly distinguishable and might be ascribed to CuO (Fig. 3). Indeed, STEM energy dispersive X-ray spectroscopy (STEM-EDXS) confirms the

presence of Cu-rich aggregates that are correlated with well-visible crystallites. These particles come out from the silica matrix, often sandwiches between spherical silica particles (Fig. 3A and 3C). The morphology of the latter remains unaffected upon impregnation (Fig. 1S). In fact, focusing on the smooth silica microspheres (away from the Cu aggregates), EDX spectroscopy reveals a fixed copper amount (Fig. S1(D)), equal to ≈ 3.0 wt.%, for I-Cu5Si, I-Cu7.4Si, and I-Cu9.1Si. This agrees with XRD results, where the intensity of CuO peaks is very high for I-Cu7.4Si and I-Cu9.1Si specimens, due to the presence of isolated CuO crystals outside of the silica spheres. To sum up, starting from I-Cu5Si, only a fraction of the copper is introduced into the silica microspheres by means of the impregnation step and a significant fraction accumulates outside of the support particles, in the form of CuO crystals.

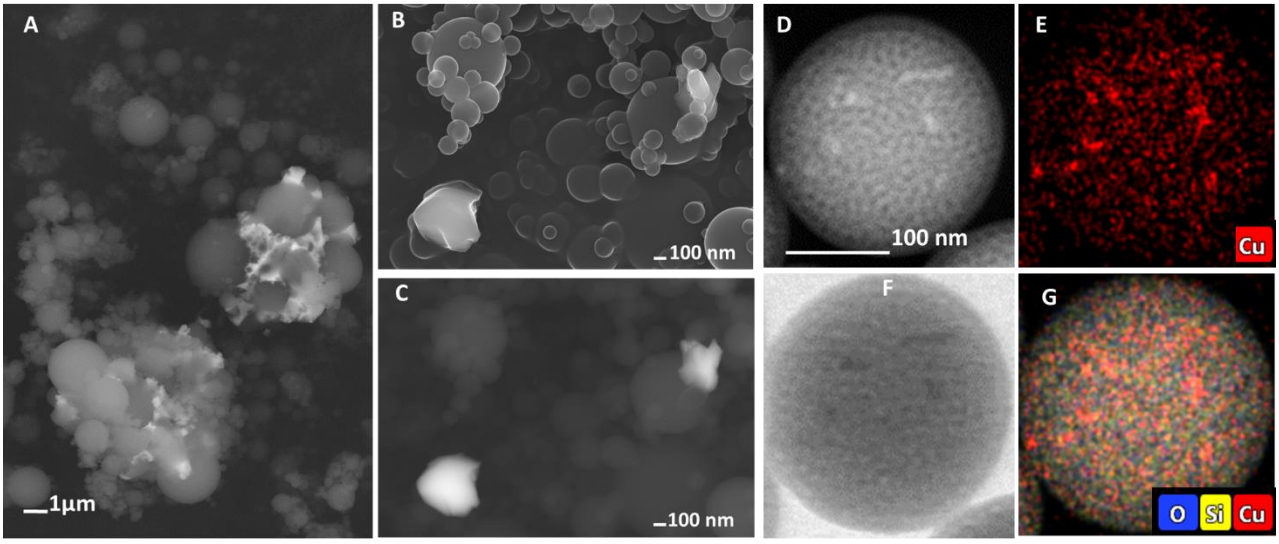

Figure 3: FE-SEM micrographs obtained on I-Cu7.4Si (A, C using the BSE signals, and B using the SE signal) and STEM images obtained on I-Cu5Si (D in dark field, E = Cu mapping, F in bright field, G = O, Si, Cu mapping.

For aerosol-made catalysts (see the example of A-Cu7.4Si in Fig. 4 and other images for A-Cu5Si in ESI, Fig. S2), FE-SEM microphotographs do not reveal the presence of copper-containing aggregates. This is in full agreement with XRD analyses. Moreover, by looking at EDX analysis for A-catalysts, the copper amount into the spheres agrees with the total Cu amount in the specimen (Fig. S2, F-G).

Thus, in agreement with FE-SEM microphotographs, it is confirmed that all the copper is incorporated into the silica microspheres. Elemental mapping by means of STEM-EDXS unambiguously confirms the homogeneous distribution of copper throughout the silica microspheres (Fig. 4).

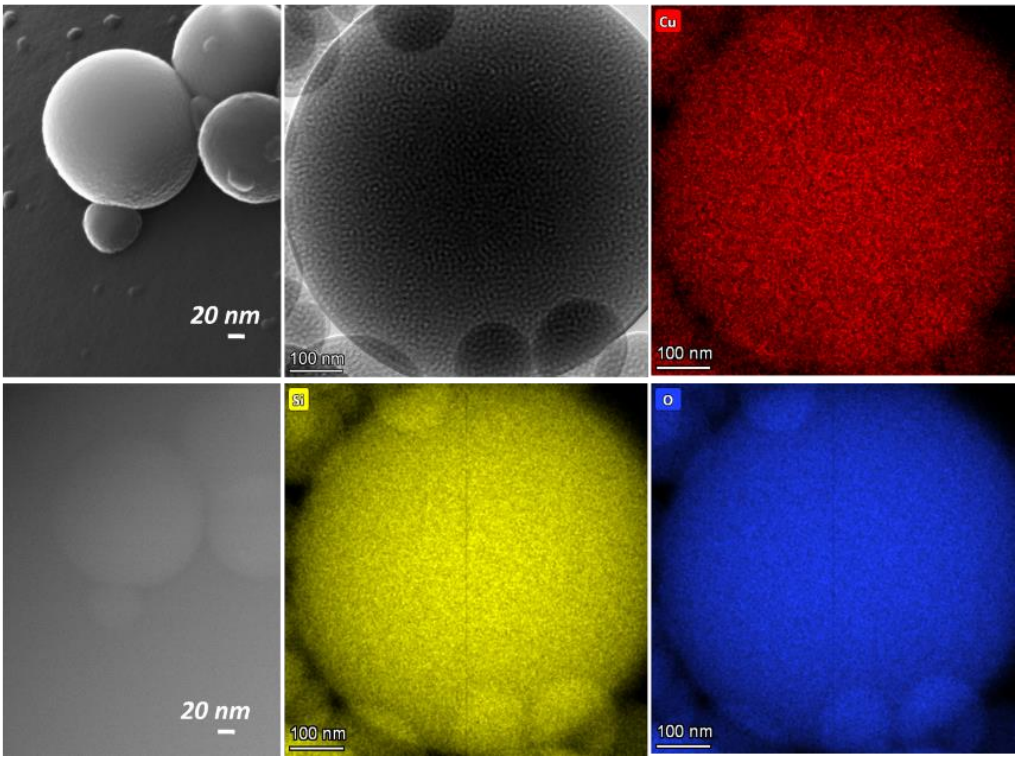

Figure 4: FE-SEM micrographs of A-Cu7.4Si using SE (left, top) and BSE (left, bottom), STEM images of A-Cu7.4Si with elemental mapping (right).

Insight on surface copper chemical state has been obtained by X-ray photoelectron spectroscopy (XPS) (Table S1 and Fig. 5). In agreement with the literature [44], Cu $2p_{3/2}$, Cu $2p_{1/2}$ peaks are found at ~933.3 eV and ~952.5 eV, accompanied by the shake-up satellite peaks (~943 eV and ~963 eV), indicating the presence of CuO (Cu^{2+} with a d^9 electron configuration), in agreement with the adopted synthetic route (calcination in air) and with XRD results. As already reported [45], two contributions can be seen for Cu $2p_{3/2}$, indicating the existence of two Cu (II) species with different chemical environment at the catalyst surface. The first one at ~933 eV is typically due to bulk-like CuO species

while the second feature at higher binding energy (~936 eV) is indicative of well dispersed Cu (II) interacting with the silica network. This may suggest the presence of -Cu-O-Si- species (i.e. well dispersed CuO and or copper phyllosilicate-like species). While this feature at 936 eV is also seen in impregnated catalysts, as shown in table 1S its intensity is much smaller than in aerosol-made catalysts, pointing again to a higher dispersion of copper via the AASG synthesis procedure. In fact, for A-catalysts upon increasing of the loading we linearly increase the surface Cu concentration (ESI, Fig. S3) while over impregnated catalysts there is no increment upon Cu loading. According to microscopy characterization and XRD patterns, this means that via impregnation only a certain amount of Cu is introduced into the pores of the silica microspheres and well dispersed at the surface. After that, Cu start to heavily aggregate without further increasing Cu superficial concentration.

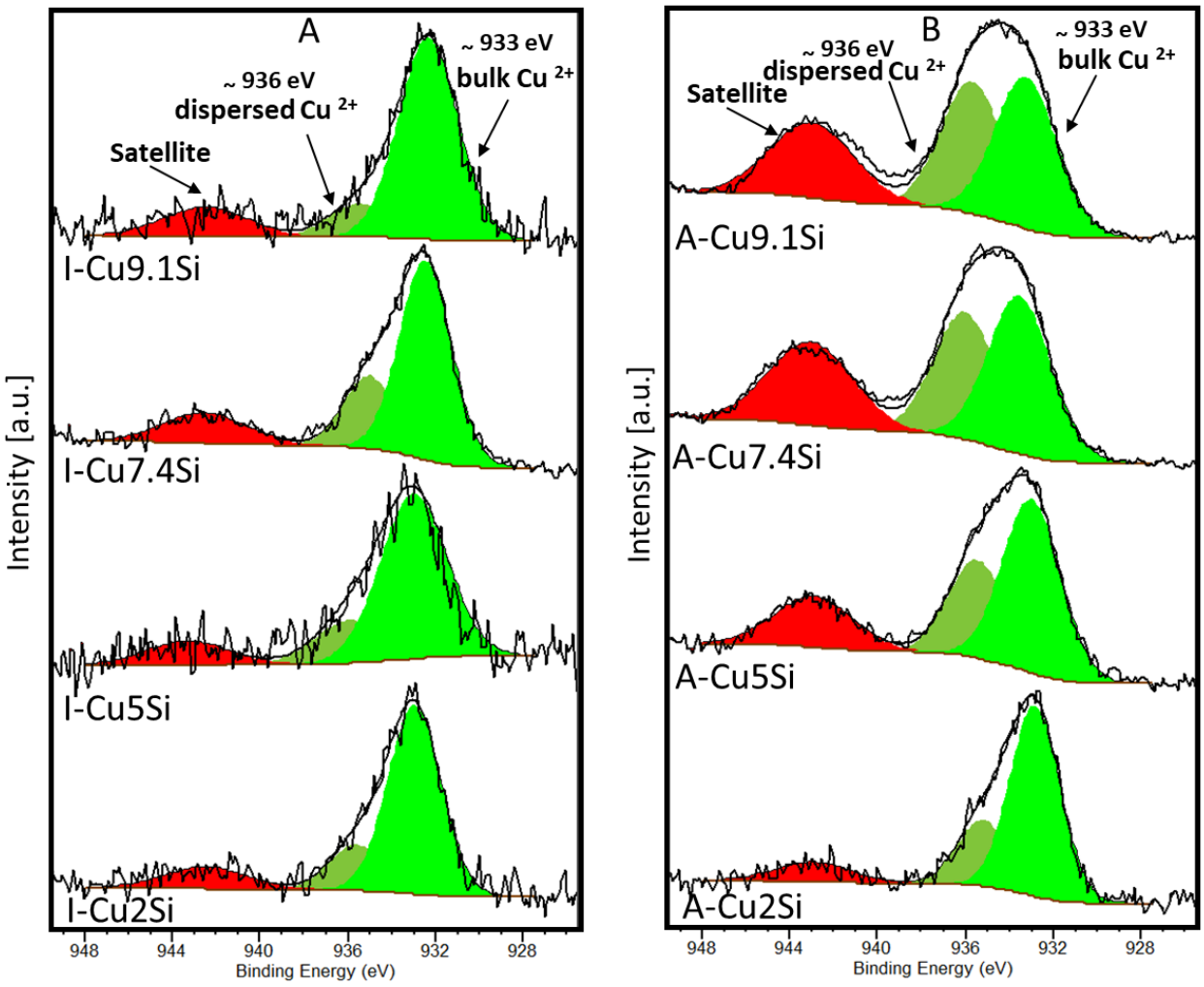

Figure 5: High-resolution XPS spectra of Cu $2p_{3/2}$ species on fresh I-catalysts (A) and A-catalysts (B).

H_2-TPR measurements were performed on A-Cu9.1Si and I-Cu9.1Si to probe copper accessibility and reducibility (Fig. S4). The hydrogen consumption for I-Cu9.1Si was 1.37 mmol H_2/g_{cat}, matching closely the amount of Cu present in the sample (1.26 mmol Cu/g_{cat}) and indicating the accessibility of Cu. For A-Cu9.1Si, 1.07 mmol H_2/g_{cat} of hydrogen was consumed, slightly lower than the actual Cu loading is 1.30. Thus, most of the copper species are reduced, even if it is likely that a small fraction of copper species remains inaccessible (trapped in the silica matrix). At the same time, copper reduction occurs at lower temperature in A-Cu9.1Si, as compared to I-Cu9.1Si. This easier reduction suggests that CuO nanoparticles are smaller in the A-catalyst. [46]

FT-IR spectra featured the characteristic features of amorphous silica absorption bands for both series of catalysts. The IR spectrum of silica is characterized by the bands assigned to the Si-O-Si asymmetric stretching (ν_1 = 1091 cm^{-1} with the corresponding pronounced shoulder at 1230 cm^{-1}), the Si-O stretching of SiOH group (968 cm^{-1}), the coupled Si-O-Si symmetric stretching/in plane bending (ν_2 = 803 cm^{-1}), and **the** corresponding out of plane bending (rocking) mode (ν_3 = 467 cm^{-1}) [47]. The spectrum obtained for the bare aerosol-made silica support is almost unchanged after impregnation of copper, showing that in this case the bulk silica is not significantly perturbed. In contrast, in the case of A-CuXSi catalysts, the position of the ν_1 mode is shifted to 1085 cm^{-1}, indicating that in this case the bulk is perturbed, probably because of the formation of Cu species in strong interaction with the silica network [48,49].

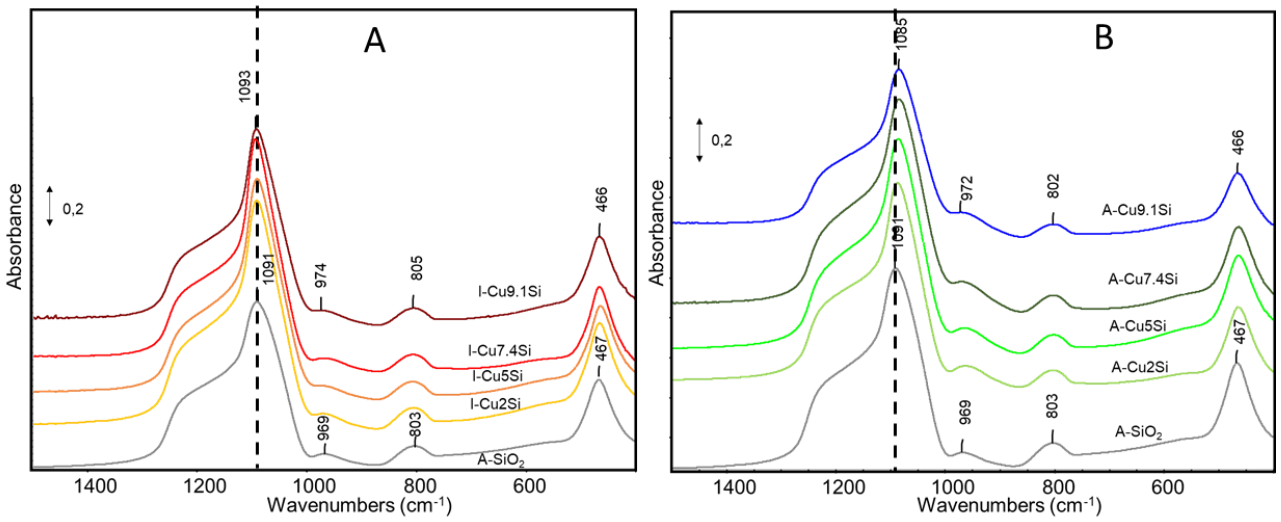

352

353 **Figure 6:** FTIR skeletal spectra (KBr pressed disks) of the fresh I- (A) and A- (B) catalysts.

354

355 UV-vis spectroscopy (Fig. S5) indicated – for both catalysts' series – that the absorption in the far
356 UV region (band in the range 200-250 nm) increases when the Cu loading increases, owing to the
357 charge transfer (CT) transition O^{2-} (2p) → Cu^{2+} (3d). Also, an additional broad absorption is detected
358 at the opposite limit of the visible range, due to the d → d transitions in dispersed Cu^{2+}. In the case
359 of A-CuXSi samples the intensity of both absorptions increases as a function of copper loading, with
360 a linear trend (see function in Figure S3). In parallel, the maximum of the d → d transition tends to
361 shift to lower wavelengths. This suggests that the nature of copper species is essentially always of the
362 same nature with increasing loading, the shift of the d → d transition being likely due to the decreasing
363 distance between the dispersed copper centres. In the spectra of I-CuXSi samples, at the highest
364 loading, the shape of the absorption band due to the d → d transitions of dispersed Cu^{2+} ions are
365 modified, suggesting that an additional absorption grows due to the d → d transition in bulk CuO.
366 This is fully consistent with the appearance of CuO diffraction peaks in the XRD pattern of these
367 samples. The linear trend between the specific absorption intensities and the copper loading (as
368 described above for A-catalysts) is verified also for I-Cu2Si and I-Cu5Si but not for I-Cu7.4Si and I-
369 Cu9.1Si, suggesting a more accentuated heterogeneity of these catalysts in terms of Cu speciation.

370 *3.2 Ethanol dehydrogenation*

371 Before being tested in the ethanol dehydrogenation reaction, the catalysts were pre-reduced in situ in
372 the reactor. For the sake of completeness, XRD data of pre-reduced catalysts are introduced in Figure
373 S6, showing effective catalyst reduction by production of metallic copper particles for all catalysts
374 (above 2 wt% Cu). Crystal sizes evaluation, carried out on the most intense peak ($2\theta = 35.6°$) by
375 means of the Scherrer equation, indicated the presence of Cu particles around 35 nm for the
376 impregnated catalysts. For aerosol-made catalysts, on the other hand, crystal size evaluation is not
377 possible because the peaks are broad and weak. These pattern features suggest that upon pre-reduction
378 Cu remains highly dispersed throughout the silica spheres at a nanometric scale.

379 In Figure 7, catalytic performances achieved over investigated materials are summarised in terms of
380 ethanol conversion and acetaldehyde selectivity. Over impregnated catalysts, the lowest conversion
381 values are found for I-Cu2Si, achieving almost 20% at 573 K. The highest conversion performances
382 are reached by I-Cu5Si, showing already 54% ethanol conversion at 573 K. However, further
383 increasing the Cu loading leads to a marked drop in performance, both in terms of conversion and in
384 terms of selectivity. The drastic drop in selectivity is particularly marked for the catalysts with the
385 highest Cu loading. This appears in line with the characterization survey that indicated a marked
386 aggregation of large CuO (Cu, after reduction) in these high-loading samples prepared by
387 impregnation. Full selectivity is obtained at 473 K and high selectivity (97%) is maintained at higher
388 temperatures for the catalysts with the lowest loading. However, the two catalysts with the highest
389 Cu loading show a marked drop in acetaldehyde selectivity when the temperature was increased to
390 523 K and higher (down to 86% at 673 K). Selectivities to diethyl ether and ethylene are reported in
391 Fig. S7 A.

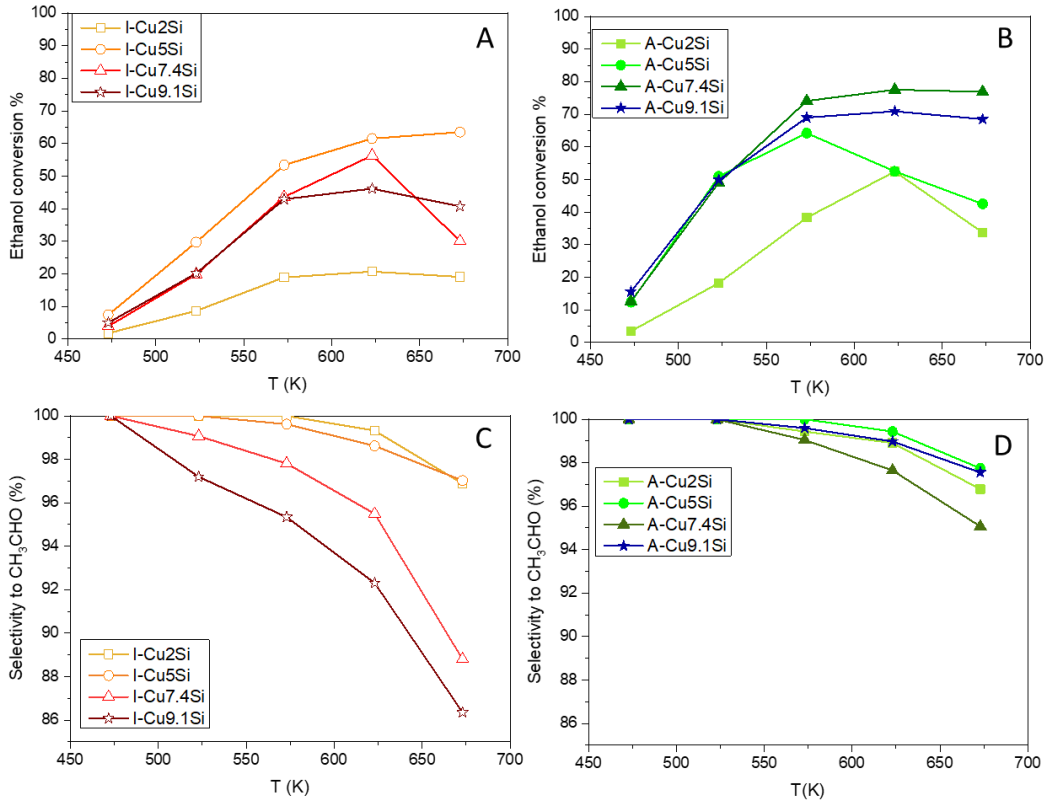

Figure 7: Ethanol conversion (A, C) and acetaldehyde selectivity (B, D) obtained with I-catalysts and A-catalysts, as a function of reaction temperature. Performances are measured by maintaining each reaction temperature constant for 1 hour, from 473 to 673 K.

In comparison with impregnated catalysts, A-CuXSi catalysts reached higher conversion. Performance increases with the Cu loading, up to A-Cu7.4Si, then were slightly lower over A-Cu9.1Si. In particular, at low temperatures aerosol-made catalysts feature almost double catalytic activity when compared to the most performant I-sample, and increased acetaldehyde selectivity with respect to I-catalysts (ESI, Fig. S7, A). These materials reached a plateau in terms of conversion above 573 K (Fig. 7C). Only a slight decrease in the selectivity (from full selectivity to ~97%) to acetaldehyde is observed when increasing the reaction temperature, due to the occurrence of ethanol dehydration to ethylene (ESI, Fig. S7, B).

A recent review on the topic allows comparing these catalysts with the state of the art [26], even if it must be stressed that operating conditions often diverge significantly from one study to another. Apart from one Cu/SiO_2 catalyst reported by Zhang et al.[48] using a relatively high copper amount and a much lower GHSV, the catalysts shown in the present work clearly outcompete all other Cu-silica formulations [26]. Beyond silica, looking at $Cu\text{-}ZnAl_2O_4$ as one the most intensively studied catalysts, we can compare with our recent results, obtained in very similar reaction conditions and with similar copper loading [50]. A-Cu7.4Si shows comparable, or slightly higher, ethanol conversion values in the entire temperature range 573 K-673 K. Furthermore, it seems to be more active at lower temperature (i.e. 49% vs 34% at 523 K).

Looking at the catalytic performances shown in Figure 7, for many of the prepared materials i.e. I-Cu7.4Si, I-Cu9.1Si, A-Cu5Si and A-Cu2Si a drop in the ethanol conversion values can be seen at the highest temperatures, suggesting that catalyst deactivation is occurring. This is also confirmed looking at conversion values versus time plots (ESI-Fig. S7, C, D) that systematically show a decreasing trend during each temperature dwelling. Previous studies pointed out that both copper sintering and carbon deposition can slow down catalytic ethanol dehydrogenation [51–53]. Thus, to shade some light on the possible deactivation causes, spent catalysts were characterized, as discussed in the next paragraph.

3.3 Spent catalysts characterization

XRD patterns of the catalysts after ethanol conversion experiments are reported in Figure 8. In almost all cases, the peaks of metallic copper (cF4-Cu, PCD ref. 1146504) are detected as the main crystalline phase, together with the appearance of characteristic peaks of Cu_2O (cP6, PCD ref. 1831225) phase. The presence of oxidized Cu species might be due to copper oxidation at the expenses of water arising from ethanol dehydration to ethylene [54] or as well to slight oxidation occurring in the presence of air during the handling of the powders. I-catalysts generally reveal a clear bigger crystal size (i.e. 48 and 10 nm for I-Cu9.1Si and A-Cu9.1Si) respect to the aerosol made ones.

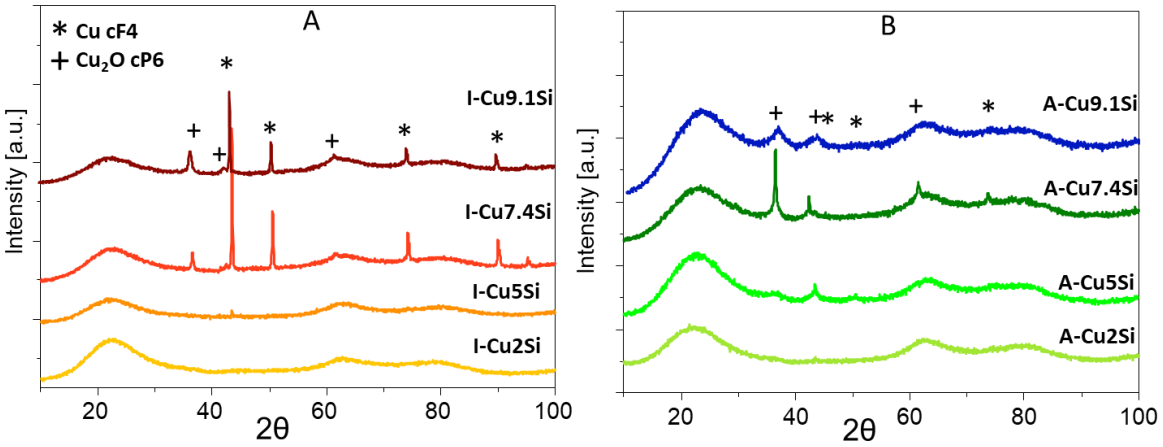

Figure 8: XRD patterns of spent catalysts after catalytic measurements (inset A: I-catalysts; inset B: A-catalysts).

FE-SEM characterization of spent catalysts is reported in Figure 9. In impregnated catalysts, copper-containing particles are visible and appear bigger than in the fresh catalysts. This shows that sintering occurred upon exposure to reaction conditions. Impregnated catalysts show a remarkable high number of copper rich particles that apparently grew in the intraparticle spaces and around small silica particles (Figure 9 A, B). Remarkably, FE-SEM characterization of the A-catalysts (Fig.9 C, D) reveal that upon the same catalytic test conditions, no bright aggregates are detected. The absence of heavy sintering can be interpreted as a sign of a stronger intimacy between the Cu species (nanoparticles) and the silica network, owing to of the aerosol-based method.

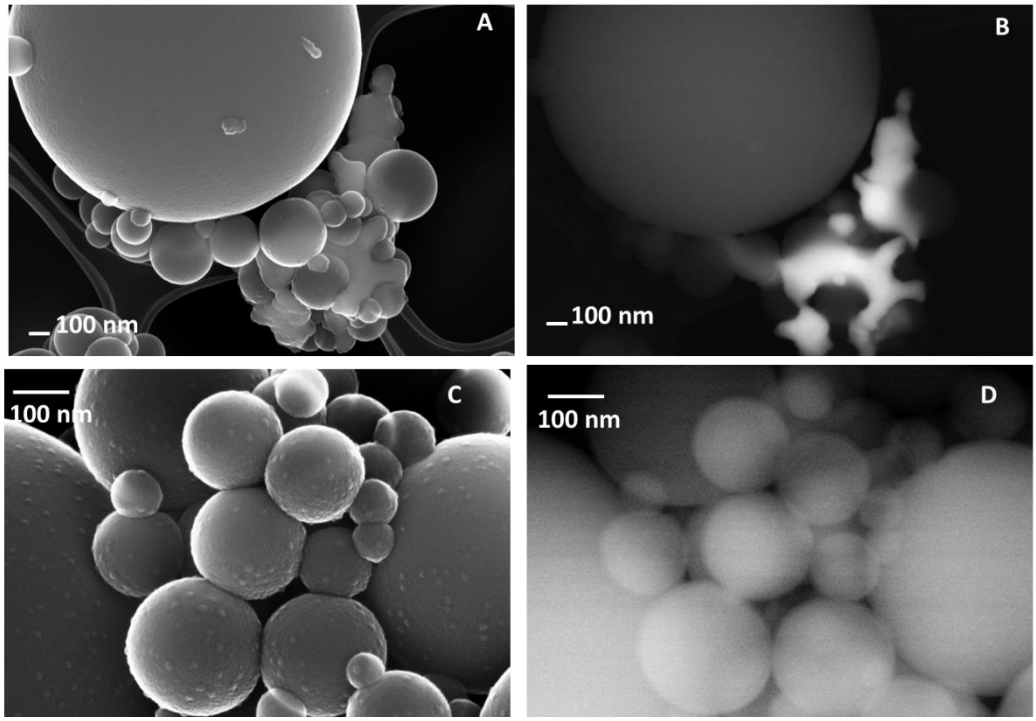

Figure 9: FE-SEM micrographs of spent ICu5Si (A, B) and Cu5Si (C, D) catalysts after the catalytic test (473-673 K). A and C are SE signals. B and D are BSE signals.

TGA analyses for all spent catalysts are reported in Figure S8. TGA of the freshly prepared (not calcined) pristine silica is also provided (Figure S9) as a benchmark to show that the surfactant is fully removed before 700 K, i.e. lower than calcination temperature (823 K). So, the mass losses detected on the spent catalysts account for carbonaceous materials accumulated during reaction. Figure 10, shows the MS signal for m/z=44 (CO_2 evolving from carbon oxidation). For all the materials two peaks are found at 530-560 K and 760 K accounting for two different carbon species deposed over catalysts during reaction. The first mass loss can be due to the presence of C-O/C=O containing carbon residue [55] or amorphous carbon species [56]. It is systematically more important for A-catalysts (that are more active) as compared to I-catalysts (Fig. S8, C). The second CO_2 peak (~760 K) is attributable to the presence of graphitic-like carbon. It is again more important for A-CuXSi, especially at low Cu loading (Fig. S8, C). Fouling by carbonaceous deposit (or coke) is classically linked to the occurrence of acid-catalysed reactions (dehydration, oligomerization, condensation,

etc.). Here, using silica as an "innocent" support, we obtain catalysts that show very low and weak acidity (as shown via NH_3-TPD analyses, see Fig. S10) [57]. In addition, we do not detect the usual dehydration products (e.g. ethylene). Here, coke formation appears to be turnover-dependent: the most active catalysts accumulate more coke. While the usual acid-catalysed path to coke can not be excluded, we surmise that the carbonaceous deposit accumulates through alternative mechanism (e.g. acetaldehyde polymerization).

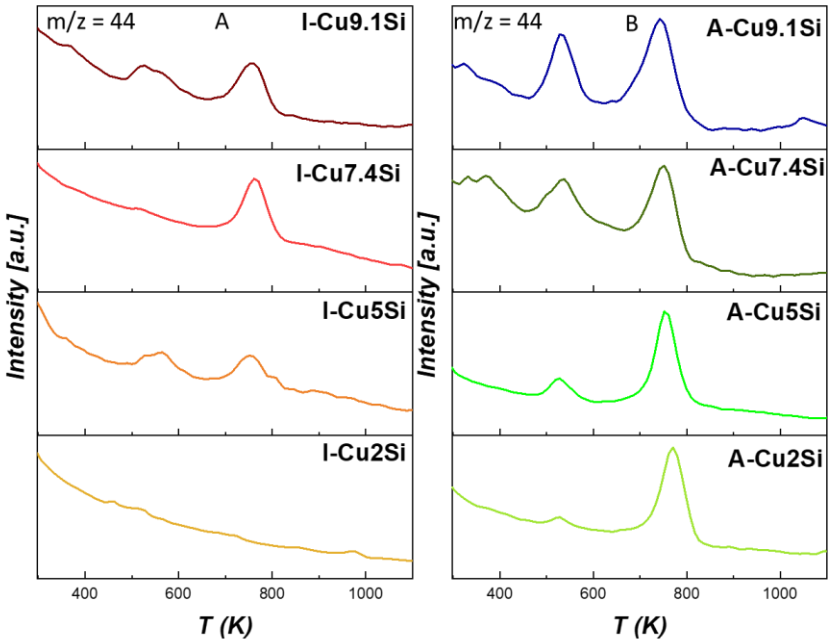

Figure 10: MS monitoring at m/z = 44 during the TGA-MS experiment on spent I-catalysts (A) and A-catalysts (B) after catalytic measures (473-673 K).

XPS measurements (Fig. S11, A, B) of the spent catalysts reveal the presence of Cu^+ and/or Cu^0 species (consistent with XRD and FE-SEM characterizations) with clear peaks at 932-933 eV (Cu $2p_{3/2}$ orbitals) and 954 eV (Cu $2p_{1/2}$ orbitals) [58]. It should be noted that partial re-oxidation can occur during handling which complicates the analysis of the Cu oxidation state in spent catalysts. However, it appears clearly that the Cu/Si ratio tends to decrease after catalytic reaction (Table S3). Causes may be both copper sintering and/or selective coke deposition on copper particles. At this stage of the study is impossible to determine which cause of deactivation is predominant but certainly the

consequence, as suggested in literature [58,59], is a reduction of active phase sites at the surface. To further investigate the coke deposition phenomenon (Fig. S11, C, D and Tables S4 and S5), XPS peaks for C1s region was investigated for both fresh and spent catalysts. The surface carbon concentration was found to increase in all spent catalysts, as compared to the fresh counterparts, confirming carbonaceous species deposition. The C1s peak was further decomposed into four contributions: O=C-O (~ 289 eV), C=O/O-C-O (~288-289 eV), C-O (~286 eV), C-(C, H) (~284.8-285 eV) [60]. Comparing fresh and exhausts analyses, the C=O/O-C-O and C-O components remain stable among the different catalysts. Probably underlining the adventitious nature of these species. Components C-(C, H), referred to aliphatic carbon, is more subjected to a variation among the spent catalysts. Considering the components of the C1s peak, it seems that aliphatic carbon species are predominant. This probably confirms the presence of coke with a main C-C-C_n pattern, probably deriving from oligomerized carbonaceous species, in fully agreement with exhaust TGA-MS analyses on spent catalysts. Finally, no satellite peaks due to π-π* bond (BE > 290 eV) are found, so extended delocalised electrons derived structures (i.e. aromatic species) [61] can be excluded. Thus, we suggest that the carbonaceous deposit that is formed during reaction is mainly composed of amorphous/polymeric coke. Finally, globally looking at the surface carbon concentration over the spent catalysts (ESI, Fig. S12), it seems to be independent of the copper loading for A-catalysts. Instead, over the impregnated ones there is a clear negative trend upon Cu increasing loading. Being that the most active sites are at the border between the support and the nanoparticle, it seems to be present a correlation between Cu crystallites dimensions, catalytic activity and coke deposition. In fact, over impregnated catalysts higher is the loading, and then, proportionally, the crystal size, lower is the coke deposition. Instead, over A-catalysts, where dimensional variation of nanoparticle is less marked, coke deposition seems to be constant.

3.4 Effect of time on stream, deactivation, and rejuvenation

The stability of A-Cu7.4Si was tested at 523 K (an industrially relevant operation temperature, where selectivity for acetaldehyde is high). During 500 min on stream, the selectivity remained complete (Fig. S13). Conversion declined slowly (from 46% to 36%), indicating progressive deactivation. To better highlight the difference between I- and A-catalysts, we also applied stability tests at a slightly higher temperature. A-Cu7.4Si and I-Cu7.4Si catalysts were tested at 573 K for 500 min (Fig. 11 A). I-Cu7.4Si starts at a conversion of 39%. A-Cu7.4Si reaches a conversion of 55 % (the test was done with 40 mg of catalyst instead of 50 mg, so that the initial conversion is in the same range for both catalysts). Both catalysts showed total selectivity to acetaldehyde. Then, conversion slowly declines with time on stream, tending to a dwelling after 400 minutes. Meanwhile, however, selectivity remains at 100%. In the course of this stability test, the yield of acetaldehyde is divided by ~4 with I-Cu7.4Si (down to ~11%), while it is only divided by a factor 2 (down to ~24%) with A-Cu7.4Si.

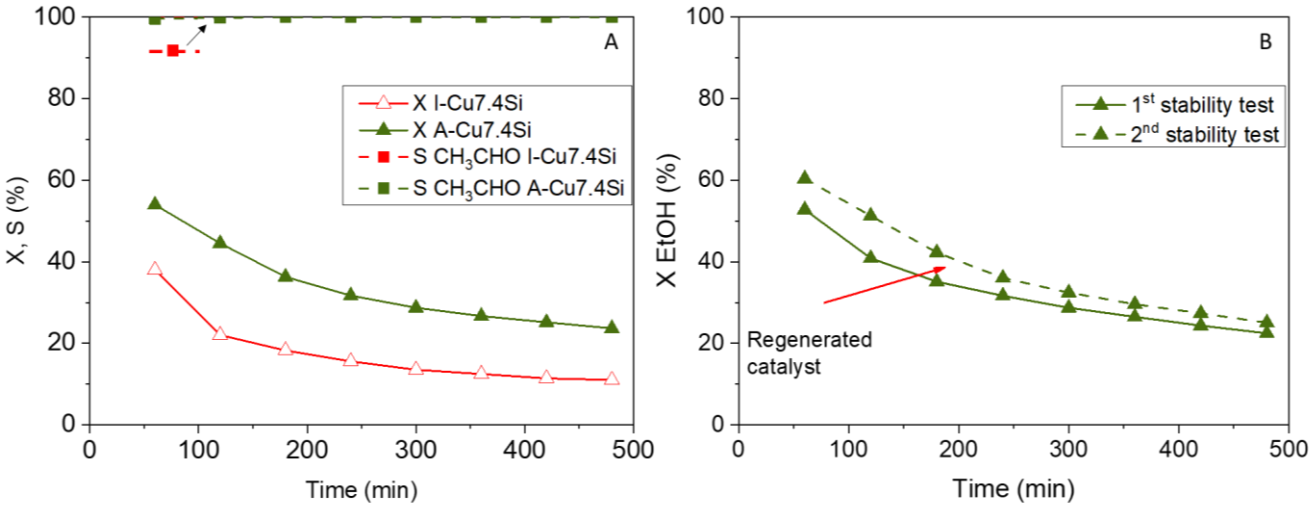

Figure 11. (A) Stability tests over A-Cu7.4Si and I-Cu7.4Si with ethanol conversion and acetaldehyde selectivity values. (B) stability test and 2nd stability test, on A-Cu7.4Si, after rejuvenation step (mild oxidative treatment) in terms of ethanol conversion.

FE-SEM microphotographs of I-catalyst post stability test (Fig. 12 A, B) reveal a large number of bright particles (Cu) that aggregate outside of the silica spheres. Thus, it is clear that, although the stability test has been carried out only at 573 K (i.e. $T < T_{Tamman}$), segregation of active phase and

progressive sintering occurred. As already reported [62] atomic migration and crystallite migration (diffusion-controlled processes that occur along the surface, followed by coalescence of atoms/crystallites) are well-known deactivation causes for supported metal nanoparticles. Moreover, pronounced sintering may also occur after prolonged time on stream or/and at high temperatures, as reported by others [19], generating irreversible deactivation. This effect is very visible on the I-catalyst. On the contrary, after the same test on the A-catalyst (Fig. 12 C, D) only a small number of Cu crystallites is detected. Moreover, looking together at fresh and spent A-catalysts micrographs, no variations in Cu distribution over the support is found. This confirms a slightly reduced mobility of Cu nanoparticles in the catalyst made by aerosol. In fact, it seems reasonable to affirm that A-catalyst shows a higher resistance to coalescence because the Cu nanoparticles are truly embedded in the silica matrix (yet accessible for catalysis, so at least partially pointing towards the external surface of the pores). The fact that Cu species tend to aggregate more on the I-catalyst than on the A-catalyst is unambiguously confirmed by elemental mapping in STEM-EDXS (Fig. 12 E, F) and by XRD (Fig. S14, E, F).

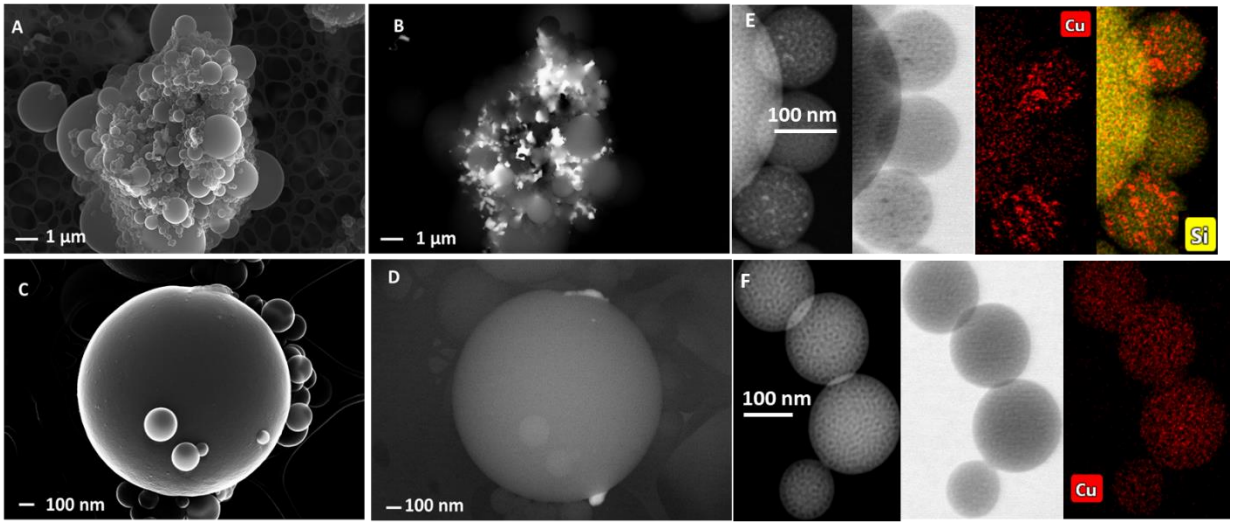

Figure 12: FE-SEM micrographs obtained on spent catalysts after the stability tests: A (SE signals), B (BSE signals) refer to ICu7.4Si while C (SE signals) and D (BSE) refer to A-Cu7.4Si. STEM images obtained on I-Cu7.4Si (E, dark field, bright field and Cu/Si mapping from left to right) and on A-Cu7.4Si (F, dark field, bright field, and Cu mapping from left to right).

All in all, both fouling by carbon deposition (ESI Fig. S14, A, B, C, D for TGA-MS), occurring on both catalysts, and more markedly on A-catalysts and Cu sintering, occurring mostly on I-catalysts and only marginally on A-catalysts, can be the main cause of the progressive deactivation. To understand whether the carbon deposition was the major source for the deactivation or not, a rejuvenation was attempted by applying an oxidative treatment (up to 788 K) on the best catalyst (i.e. A-Cu7.4Si) after the stability test. Surprisingly, the 2nd stability test (after the rejuvenation) reached conversion values slightly higher than in the first test (Fig. 11 B) and total selectivity to acetaldehyde was maintained. The origin of this slight increase in activity would require further investigations. Yet, this experiment reveals that the main limiting factor for catalyst stability is the progressive coke deposition [63]. However, the carbonaceous deposit can be easily removed using a mild oxidative treatment.

4. Conclusions

Simple and direct synthesis method relying on the aerosol-assisted sol-gel (AASG) process can be utilized to prepare efficient Cu-based catalysts for the non-oxidative dehydrogenation of (bio)ethanol to acetaldehyde. The process leads to spherical and mesostructured silica-based microparticles with highly dispersed Cu species. From a detailed characterization survey, it comes up that preparation methods strongly influence the catalytic properties. In fact, our experimental data suggest that respect to catalysts fabricated by impregnation with one pot made ones is possible to obtain i) smaller nanoparticles, ii) a higher dispersion of Cu at the surface iii) a stronger intimacy between the active phase and the support. A-catalysts present better dehydrogenation performance respect to impregnated ones, in particular at 573 K. Characterization of spent catalysts reveals that deactivation occurs by copper segregation and coke deposition. The main cause of catalyst deactivation seems to be the second one. However, over A-catalysts, where it has been proved that sintering has a limited

effect, carbon deposition can be easily reversed with a mild oxidative treatment rejuvenating the catalytic activity.

Acknowledgements

GP acknowledges University of Genova for fundings to carry out the research period at UCLouvain and François Devred, Pierre Eloy and Jean François Statsyns for their technical assistance. PR acknowledges funding from INSTM in the frame of the project INSTM19GE1 entitled “Synthesis and characterization of nanostructured catalysts for renewable’s conversion to chemicals”. DPD thanks the Francqui Foundation for the Francqui Research professor chair.

References

(1) Zabed, H.; Sahu, J. N.; Suely, A.; Boyce, A. N.; Faruq, G. Bioethanol Production from Renewable Sources: Current Perspectives and Technological Progress. *Renewable and Sustainable Energy Reviews* **2017**, *71* (January), 475–501. https://doi.org/10.1016/j.rser.2016.12.076.

(2) Sun, J.; Wang, Y. Recent Advances in Catalytic Conversion of Ethanol to Chemicals. *ACS Catal* **2014**, *4* (4), 1078–1090. https://doi.org/10.1021/cs4011343.

(3) Garbarino, G.; Pampararo, G.; Phung, T. K.; Riani, P.; Busca, G. Heterogeneous Catalysis in (Bio)Ethanol Conversion to Chemicals and Fuels: Thermodynamics, Catalysis, Reaction Paths, Mechanisms and Product Selectivities. *Energies 2020, Vol. 13, Page 3587* **2020**, *13* (14), 3587. https://doi.org/10.3390/EN13143587.

(4) Fleischmann, G.; Jira, R.; Bolt, H. M.; Golka, K. Acetaldehyde. In *Ullmann’s Encyclopedia of Industrial Chemistry*; Wiley-VCH Verlag GmbH & Co. KGaA: Weinheim, Germany, 2000. https://doi.org/10.1002/14356007.a01_031.

(5) Church, J. M.; Joshi, H. K. Acetaldehyde by Dehydrogenation of Ethyl Alcohol. *Ind Eng Chem Res* **1951**, *43* (8), 1804–1811. https://doi.org/10.1021/ie50500a035.

(6) Huang, Y.; Wang, B.; Yuan, H.; Sun, Y.; Yang, D.; Cui, X.; Shi, F. The Catalytic Dehydrogenation of Ethanol by Heterogeneous Catalysts. *Catal Sci Technol* **2021**, *11* (5), 1652–1664. https://doi.org/10.1039/d0cy02479a.

(7) Sato, A. G.; Volanti, D. P.; Meira, D. M.; Damyanova, S.; Longo, E.; Bueno, J. M. C. Effect of the ZrO_2 Phase on the Structure and Behavior of Supported Cu Catalysts for Ethanol Conversion. *J Catal* **2013**, *307*, 1–17. https://doi.org/10.1016/j.jcat.2013.06.022.

(8) Freitas, I. C.; Damyanova, S.; Oliveira, D. C.; Marques, C. M. P.; Bueno, J. M. C. Effect of Cu Content on the Surface and Catalytic Properties of Cu/ZrO_2 Catalyst for Ethanol Dehydrogenation. *J Mol Catal A Chem* **2014**, *381*, 26–37. https://doi.org/10.1016/j.molcata.2013.09.038.

(9) Sato, A. G.; Volanti, D. P.; de Freitas, I. C.; Longo, E.; Bueno, J. M. C. Site-Selective Ethanol Conversion over Supported Copper Catalysts. *Catal Commun* **2012**, *26*, 122–126. https://doi.org/10.1016/J.CATCOM.2012.05.008.

(10) Hanukovich, S.; Dang, A.; Christopher, P. Influence of Metal Oxide Support Acid Sites on Cu-Catalyzed Nonoxidative Dehydrogenation of Ethanol to Acetaldehyde. *ACS Catal* **2019**, *9* (4), 3537–3550. https://doi.org/10.1021/acscatal.8b05075.

(11) Vidya Sagar, G.; Venkat Ramana Rao, P.; Srikanth, C. S.; R Chary, K. V. Dispersion and Reactivity of Copper Catalysts Supported on Al_2O_3-ZrO_2. **2006**. https://doi.org/10.1021/jp0575153.

(12) DeWilde, J. F.; Czopinski, C. J.; Bhan, A. Ethanol Dehydration and Dehydrogenation on γ-Al_2O_3: Mechanism of Acetaldehyde Formation. *ACS Catal* **2014**, *4* (12), 4425–4433. https://doi.org/10.1021/cs501239x.

(13) Pampararo, G.; Garbarino, G.; Riani, P.; Villa García, M.; Sánchez Escribano, V.; Busca, G. A Study of Ethanol Dehydrogenation to Acetaldehyde over Supported Copper Catalysts: Catalytic Activity, Deactivation and Regeneration. *Appl Catal A Gen* **2020**, *602* (June), 117710. https://doi.org/10.1016/j.apcata.2020.117710.

(14) Garbarino, G.; Riani, P.; Villa García, M.; Finocchio, E.; Sánchez Escribano, V.; Busca, G. A Study of Ethanol Conversion over Zinc Aluminate Catalyst. *Reaction Kinetics, Mechanisms and Catalysis* **2018**, *124* (2), 503–522. https://doi.org/10.1007/s11144-018-1395-z.

(15) Garbarino, G.; Riani, P.; Villa García, M.; Finocchio, E.; Sanchez Escribano, V.; Busca, G. A Study of Ethanol Dehydrogenation to Acetaldehyde over Copper/Zinc Aluminate Catalysts. *Catal Today* **2019**, No. August 2018, 0–1. https://doi.org/10.1016/j.cattod.2019.01.002.

(16) Liu, H.; Jiang, Y.; Zhou, R.; Chang, Z.; Hou, Z. Co-Production of Hydrogen and Acetaldehyde from Ethanol over a Highly Dispersed Cu Catalyst. *Fuel* **2022**, *321*, 123980. https://doi.org/10.1016/J.FUEL.2022.123980.

(17) Simón, E.; Rosas, J. M.; Santos, A.; Romero, A. Study of the Deactivation of Copper-Based Catalysts for Dehydrogenation of Cyclohexanol to Cyclohexanone. *Catal Today* **2012**, *187* (1), 150–158. https://doi.org/10.1016/J.CATTOD.2011.10.010.

(18) Ob-eye, J.; Praserthdam, P.; Jongsomjit, B. Dehydrogenation of Ethanol to Acetaldehyde over Different Metals Supported on Carbon Catalysts. *Catalysts* **2019**, *9* (1), 66. https://doi.org/10.3390/catal9010066.

(19) Conesa, J. M.; Morales, M. V.; López-Olmos, C.; Rodríguez-Ramos, I.; Guerrero-Ruiz, A. Comparative Study of Cu, Ag and Ag-Cu Catalysts over Graphite in the Ethanol Dehydrogenation Reaction: Catalytic Activity, Deactivation and Regeneration. *Appl Catal A Gen* **2019**, *576*, 54–64. https://doi.org/10.1016/j.apcata.2019.02.031.

(20) Morales, M. V.; Asedegbega-Nieto, E.; Bachiller-Baeza, B.; Guerrero-Ruiz, A. Bioethanol Dehydrogenation over Copper Supported on Functionalized Graphene Materials and a High Surface Area Graphite. *Carbon N Y* **2016**, *102*, 426–436. https://doi.org/10.1016/j.carbon.2016.02.089.

(21) Hao, Y.; Zhao, D.; Liu, W.; Zhang, M.; Lou, Y.; Wang, Z.; Tang, Q.; Yang, J. Uniformly Dispersed Cu Nanoparticles over Mesoporous Silica as a Highly Selective and Recyclable Ethanol Dehydrogenation Catalyst. *Catalysts* **2022**, *12* (9), 1049. https://doi.org/10.3390/CATAL12091049/S1.

(22) Finger, P. H.; Osmari, T. A.; Costa, M. S.; Bueno, J. M. C.; Gallo, J. M. R. The Role of the Interface between Cu and Metal Oxides in the Ethanol Dehydrogenation. *Appl Catal A Gen* **2020**, *589*, 117236. https://doi.org/10.1016/J.APCATA.2019.117236.

(23) Ohira, M.; Liu, H.; He, D.; Hirata, Y.; Sano, M.; Suzuki, T.; Miyake, T. Catalytic Performance and Reaction Pathways of Cu/SiO_2 and ZnO/SiO_2 for Dehydrogenation of Ethanol to Acetaldehyde. *J. Japan Pet. Inst.* **2018**, *61* (4), 205–212. https://doi.org/10.1627/JPI.61.205.

(24) Liu, H.; Chang, Z.; Fu, J.; Hou, Z. A CuZn-BTC Derived Stable $Cu/ZnO@SiO_2$ Catalyst for Ethanol Dehydrogenation. *Appl Catal B* **2023**, *324*, 122194. https://doi.org/10.1016/J.APCATB.2022.122194.

(25) Finger, P. H.; Osmari, T. A.; Cabral, N. M.; Bueno, J. M. C.; Gallo, J. M. R. Direct Synthesis of Cu Supported on Mesoporous Silica: Tailoring the Cu Loading and the Activity for Ethanol Dehydrogenation. *Catal Today* **2020**, No. August, 1–8. https://doi.org/10.1016/j.cattod.2020.10.019.

(26) Phung, T. K. Copper-Based Catalysts for Ethanol Dehydrogenation and Dehydrogenative Coupling into Hydrogen, Acetaldehyde and Ethyl Acetate. *Int J Hydrogen Energy* **2022**, *47* (100), 42234–42249. https://doi.org/10.1016/J.IJHYDENE.2021.11.253.

(27) Volanti, D. P.; Sato, A. G.; Orlandi, M. O.; Bueno, J. M. C.; Longo, E.; Andrøs, J.; Volanti, P.; Orlandi, M. O.; Longo, E.; Sato, A G; Bueno, J. M. C.; Andrøs, J. Insight into Copper-Based Catalysts: Microwave-Assisted Morphosynthesis, In Situ Reduction Studies, and Dehydrogenation of Ethanol. *ChemCatChem* **2011**, *3* (5), 839–843. https://doi.org/10.1002/CCTC.201000462.

(28) Lu, W. D.; Wang, Q. N.; He, L.; Li, W. C.; Schüth, F.; Lu, A. H. Copper Supported on Hybrid $C@SiO_2$ Hollow Submicron Spheres as Active Ethanol Dehydrogenation Catalyst. *ChemNanoMat* **2018**, *4* (5), 505–509. https://doi.org/10.1002/CNMA.201800021.

(29) Dong, X.; Ma, X.; Xu, H.; Ge, Q. Comparative Study of Silica-Supported Copper Catalysts Prepared by Different Methods: Formation and Transition of Copper Phyllosilicate. *Catal Sci Technol* **2016**, *6* (12), 4151–4158. https://doi.org/10.1039/c5cy01965f.

(30) Twigg, M. v.; Spencer, M. S. Deactivation of Supported Copper Metal Catalysts for Hydrogenation Reactions. *Appl Catal A Gen* **2001**, *212* (1–2), 161–174. https://doi.org/10.1016/S0926-860X(00)00854-1.

(31) Yang, F.; Zhao, H.; Wang, W.; Wang, L.; Zhang, L.; Liu, T.; Sheng, J.; Zhu, S.; He, D.; Lin, L.; He, J.; Wang, R.; Li, Y. Atomic Origins of the Strong Metal–Support Interaction in Silica Supported Catalysts. *Chem Sci* **2021**, *12* (38), 12651–12660. https://doi.org/10.1039/D1SC03480D.

(32) Regalbuto, J. *Catalyst Preparation: Science and Engineering*;. CRC Press, **2007**. https://doi.org/10.1016/s1351-4180(07)70051-x.

(33) Boissiere, C.; Grosso, D.; Chaumonnot, A.; Nicole, L.; Sanchez, C. Aerosol Route to Functional Nanostructured Inorganic and Hybrid Porous Materials. *Advanced Materials* **2011**, *23* (5), 599–623. https://doi.org/10.1002/adma.201001410.

(34) Debecker, D. P.; le Bras, S.; Boissière, C.; Chaumonnot, A.; Sanchez, C. Aerosol Processing: A Wind of Innovation in the Field of Advanced Heterogeneous Catalysts. *Chem Soc Rev* **2018**, *47* (11), 4112–4155. https://doi.org/10.1039/c7cs00697g.

(35) Debecker, D. P.; Stoyanova, M.; Colbeau-Justin, F.; Rodemerck, U.; Boissiãre, C.; Gaigneaux, E. M.; Sanchez, C. One-Pot Aerosol Route to MoO_3-SiO_2-Al_2O_3 Catalysts with Ordered Super Microporosity and High Olefin Metathesis Activity. *Angewandte Chemie International Edition* **2012**, *51* (9), 2129–2131. https://doi.org/10.1002/ANIE.201106277.

(36) Kim, A.; Sanchez, C.; Haye, B.; Boissière, C.; Sassoye, C.; Debecker, D. P. Mesoporous TiO_2 Support Materials for Ru-Based CO_2 Methanation Catalysts. *ACS Appl Nano Mater* **2019**, *2* (5), 3220–3230. https://doi.org/10.1021/ACSANM.9B00518.

(37) Paris, C.; Karelovic, A.; Manrique, R.; Bras, S. le; Devred, F.; Vykoukal, V.; Styskalik, A.; Eloy, P.; Debecker, D. P. CO_2 Hydrogenation to Methanol with Ga- and Zn-Doped Mesoporous Cu/SiO_2 Catalysts Prepared by the Aerosol-Assisted Sol-Gel Process. *ChemSusChem* **2020**, *13* (23), 6409–6417. https://doi.org/10.1002/CSSC.202001951.

(38) Gabaldon, J. P.; Bore, M.; Datye, A. K. Mesoporous Silica Supports for Improved Thermal Stability in Supported Au Catalysts. *Topics in Catalysis 2007 44:1* **2007**, *44* (1), 253–262. https://doi.org/10.1007/S11244-007-0298-4.

(39) Košević, M.; Stopic, S.; Cvetković, V.; Schroeder, M.; Stevanović, J.; Panić, V.; Friedrich, B. Mixed RuO2/TiO2 Uniform Microspheres Synthesized by Low-Temperature Ultrasonic Spray Pyrolysis and Their Advanced Electrochemical Performances. *Appl Surf Sci* **2019**, *464*, 1–9. https://doi.org/10.1016/J.APSUSC.2018.09.066.

(40) P. Villars, K. C. Pearson's Crystal Data: Crystal Structure Database for Inorganic Compounds (on DVD). ASM International®: Materials Park, Ohio, USA 2020.

(41) Jacquemin, M.; Genet, M. J.; Gaigneaux, E. M.; Debecker, D. P. Calibration of the X-Ray Photoelectron Spectroscopy Binding Energy Scale for the Characterization of Heterogeneous Catalysts: Is Everything Really under Control? *ChemPhysChem* **2013**, *14* (15), 3618–3626. https://doi.org/10.1002/CPHC.201300411.

(42) Groen, J. C.; Peffer, L. A. A.; Pérez-Ramírez, J. Pore Size Determination in Modified Micro- and Mesoporous Materials. Pitfalls and Limitations in Gas Adsorption Data Analysis. *Microporous and Mesoporous Materials* **2003**, *60* (1–3), 1–17. https://doi.org/10.1016/S1387-1811(03)00339-1.

(43) Du, H.; Ma, X.; Yan, P.; Jiang, M.; Zhao, Z.; Zhang, Z. C. Catalytic Furfural Hydrogenation to Furfuryl Alcohol over Cu/SiO_2 Catalysts: A Comparative Study of the Preparation Methods. *Fuel Processing Technology* **2019**, *193* (January), 221–231. https://doi.org/10.1016/j.fuproc.2019.05.003.

(44) Gong, J.; Yue, H.; Zhao, Y.; Zhao, S.; Zhao, L.; Lv, J.; Wang, S.; Ma, X. Synthesis of Ethanol via Syngas on Cu/SiO_2 Catalysts with Balanced Cu^0-Cu^+ Sites. *J Am Chem Soc* **2012**, *134* (34), 13922–13925. https://doi.org/10.1021/JA3034153/SUPPL_FILE/JA3034153_SI_001.PDF.

(45) Gervasini, A.; Manzoli, M.; Martra, G.; Ponti, A.; Ravasio, N.; Sordelli, L.; Zaccheria, F. Dependence of Copper Species on the Nature of the Support for Dispersed CuO Catalysts. *Journal of Physical Chemistry B* **2006**, *110* (15), 7851–7861. https://doi.org/10.1021/JP056604C.

(46) Smith, M. L.; Campos, A.; Spivey, J. J. Reduction Processes in Cu/SiO_2, Co/SiO_2, and CuCo/SiO_2 Catalysts. *Catal Today* **2012**, *182* (1), 60–66. https://doi.org/10.1016/J.CATTOD.2011.07.026.

(47) Riani, P.; Garbarino, G.; Cavattoni, T.; Busca, G. CO2 Hydrogenation and Ethanol Steam Reforming over Co/SiO_2 Catalysts: Deactivation and Selectivity Switches. *Catal Today* **2021**, *365*, 122–131. https://doi.org/10.1016/J.CATTOD.2020.05.002.

(48) Zhang, H.; Tan, H. R.; Jaenicke, S.; Chuah, G. K. Highly Efficient and Robust Cu Catalyst for Non-Oxidative Dehydrogenation of Ethanol to Acetaldehyde and Hydrogen. *J Catal* **2020**, *389*, 19–28. https://doi.org/10.1016/j.jcat.2020.05.018.

(49) Xu, C.; Chen, G.; Zhao, Y.; Liu, P.; Duan, X.; Gu, L.; Fu, G.; Yuan, Y.; Zheng, N. Interfacing with Silica Boosts the Catalysis of Copper. *Nat Commun* **2018**, *9* (1), 1–10. https://doi.org/10.1038/s41467-018-05757-6.

(50) Pampararo, G.; Garbarino, G.; Comite, A.; Busca, G.; Riani, P. Acetaldehyde Production by Ethanol Dehydrogenation over Cu-ZnAl2O4: Effect of Catalyst Synthetic Strategies on Performances. *Chem Eng Sci* **2022**, *261*, 117937. https://doi.org/10.1016/J.CES.2022.117937.

(51) Meyer, C. I.; Marchi, A. J.; Monzon, A.; Garetto, T. F. Deactivation and Regeneration of Cu/SiO_2 Catalyst in the Hydrogenation of Maleic Anhydride. Kinetic Modeling. *Appl Catal A Gen* **2009**, *367* (1–2), 122–129. https://doi.org/10.1016/j.apcata.2009.07.041.

(52) Twigg, M. V.; Spencer, M. S. Deactivation of Supported Copper Metal Catalysts for Hydrogenation Reactions. *Appl Catal A Gen* **2001**, *212* (1–2), 161–174. https://doi.org/10.1016/S0926-860X(00)00854-1.

(53) Du, H.; Ma, X.; Yan, P.; Jiang, M.; Zhao, Z.; Zhang, Z. C. Catalytic Furfural Hydrogenation to Furfuryl Alcohol over Cu/SiO_2 Catalysts: A Comparative Study of the Preparation Methods. *Fuel Processing Technology* **2019**, *193* (January), 221–231. https://doi.org/10.1016/j.fuproc.2019.05.003.

(54) Chen, Z.; Chen, J. Comparative Study of the Effect of Water on Cu/SiO_2 Catalysts Prepared by Different Methods: Structure, Hydrogenation Performance and the Promotion of Reduction Cu+ to Cu0. *ChemistrySelect* **2020**, *5* (34), 10781–10786. https://doi.org/10.1002/slct.202002545.

(55) Zhang, M.; Tan, X.; Zhang, T.; Han, Z.; Jiang, H. The Deactivation of a ZnO Doped ZrO_2 –SiO_2 Catalyst in the Conversion of Ethanol/Acetaldehyde to 1,3-Butadiene. *RSC Adv* **2018**, *8* (59), 34069–34077. https://doi.org/10.1039/C8RA06757K.

(56) Argyle, M. D.; Bartholomew, C. H. Heterogeneous Catalyst Deactivation and Regeneration: A Review. *Catalysts* **2015**, *5* (1), 145–269. https://doi.org/10.3390/catal5010145.

(57) Leistner, K.; Xie, K.; Kumar, A.; Kamasamudram, K.; Olsson, L. Ammonia Desorption Peaks Can Be Assigned to Different Copper Sites in Cu/SSZ-13. *Catal Letters* **2017**, *147* (8), 1882–1890. https://doi.org/10.1007/S10562-017-2083-8/TABLES/4.

(58) Guerrero-Ruiz, A.; Rodríguez-Ramos, I.; Siri, G. J.; Fierro, J. L. G. Joint Use of XPS and Auger Techniques for the Identification of Chemical State of Copper in Spent Catalysts. *Surface and Interface Analysis* **1992**, *19* (1–12), 548–552. https://doi.org/10.1002/sia.7401901102.

(59) Cesar, D. V.; Peréz, C. A.; Schmal, M.; Salim, V. M. M. Quantitative XPS Analysis of Silica-Supported Cu-Co Oxides. *Appl Surf Sci* **2000**, *157* (3), 159–166. https://doi.org/10.1016/S0169-4332(99)00568-1.

(60) Watts, J. F. High Resolution XPS of Organic Polymers: The Scienta ESCA 300 Database. G. Beamson and D. Briggs. 280pp., £65. John Wiley & Sons, Chichester, ISBN 0471 935921, (1992). *Surface and Interface Analysis* **1993**, *20* (3), 267–267. https://doi.org/10.1002/SIA.740200310.

(61) Kelemen, S. R.; Rose, K. D.; Kwiatek, P. J. Carbon Aromaticity Based on XPS II to II$*$ Signal Intensity. *Appl Surf Sci* **1993**, *64* (2), 167–174. https://doi.org/10.1016/0169-4332(93)90276-H.

(62) Cao, A.; Lu, R.; Veser, G. Stabilizing Metal Nanoparticles for Heterogeneous Catalysis. *Physical Chemistry Chemical Physics* **2010**, *12* (41), 13499–13510. https://doi.org/10.1039/c0cp00729c.

(63) Vargas-Hernández, D.; Rubio-Caballero, J. M.; Santamaría-González, J.; Moreno-Tost, R.; Mérida-Robles, J. M.; Pérez-Cruz, M. A.; Jiménez-López, A.; Hernández-Huesca, R.; Maireles-Torres, P. Furfuryl Alcohol from Furfural Hydrogenation over Copper Supported on SBA-15 Silica Catalysts. *J Mol Catal A Chem* **2014**, *383–384*, 106–113. https://doi.org/10.1016/j.molcata.2013.11.034.